Excited-State Vibrational Coherence in Methanol Solution of Zn^{II} Tetrakis(*N*-methylpyridyl)porphyrin: Charge-Dependent Intermolecular Mode Frequencies and Implications for Electron-Transfer Dynamics in Photosynthetic Reaction Centers

Kevin L. Dillman[†] **and Warren F. Beck***

Department of Chemistry, Michigan State University, East Lansing, Michigan 48824, United States

Received: July 12, 2010; Revised Manuscript Received: September 29, 2010

The nature of the intermolecular vibrational modes between the redox-active chromophores and the protein medium in the photosynthetic reaction center is central to an understanding of the structural origin of the quantum efficiency of the light-driven charge-separation reactions that result in storage of solar energy. In recent work on this issue, we have characterized the low-frequency vibrational coherence of Zn^{II} *meso*-tetrakis(*N*-methylpyridyl)porphyrin (ZnTMPyP) and compared it to that from bacteriochlorophyll *a* in polar solution and in the small light-harvesting subunits B820 and B777. The charge-transfer character of ZnTMPyP's π^* excited states afford us the opportunity to characterize how the intermolecular vibrational modes and potential with the surrounding medium are affected by the charge on the porphyrin macrocycle. The excited-state vibrational coherence observed with *Q*-band (S₁ state) excitation at 625 nm of ZnTMPyP in methanol solution contains dominant contributions from a pair of rapidly damped (effective damping time $\gamma < 400$ fs) components that are assigned to the hindered translational and librational porphyrin-solvent intermolecular modes. The 256 cm⁻¹ mean frequency of the intermolecular modes is significantly higher than that observed previously in the ground state, 79 cm⁻¹, with Soret-band excitation at 420 nm [Dillman et al., *J. Phys. Chem. B.* **2009**, *113*, 6127−6139]. The increased mode frequency arises from the activation of the ion−dipole and ion−induced-dipole terms in the intermolecular potential. In the ground state, the π-electron density of ZnTMPyP is mostly confined to the region of the porphyrin macrocycle. In the excited state, the π-electron density is extensively delocalized from the porphyrin out to two of the peripheral *N*-methylpyridyl rings, each of which carries a single formal charge. The charge-dependent terms contribute to a significant stabilization of the equilibrium geometry of the porphyrin−solvent complex in the excited state. In the photosynthetic reaction center, these terms will play an important role in trapping the charged products of the forward, charge-separation reactions, and the location of the bacteriopheophytin acceptor in a nonpolar region of the structure enhances the rate of the secondary charge-separation reaction.

1. Introduction

The observation of vibrational coherence in femtosecond pump−probe experiments with resonant impulsive excitation of electronic chromophores in solution[1–7] is usually assigned to coherent wavepacket motions arising from an excited-state displacement of a small number of resonance Raman-active skeletal normal modes. In several reactions of photobiological significance, excited-state wavepacket motions are crucially associated with the chromophore's progress along the reaction coordinate. Shank, Mathies, and co-workers characterized coherent wavepacket motion in retinal's torsional modes associated with the formation of the photoisomerization product state in bacteriorhodopsin and rhodopsin.[3,8–12] Champion and co-workers observed an analogous reaction-driven vibrational coherence in the ground-state out-of-plane porphyrin modes in myoglobin and cytochrome *c* following photodissociation of axial ligands.[13–15] A similar reaction was characterized by Martin, Vos, and co-workers,[16] who observed vibrational coherence in cytochrome *c* oxidase *aa₃* upon photolysis and transfer of carbon monoxide from heme *a₃* to Cu_B.

The excited-state vibrational coherence observed by Vos, Martin, and co-workers[17–25] from the excited state of the primary electron donor, P, in the purple-bacterial photosynthetic reaction center[26–28] is distinctive because the active modes have been assigned to the surrounding protein medium rather than just from the paired bacteriochlorophyll (BChl) chromophore itself. Because of their low frequencies, the protein modes would be delocalized, just as phonons are in molecular crystals, over the structures spanning the reaction center's chromophores.[17,19,24] The activationless reaction dynamics observed for the primary electron-transfer reaction in the reaction center[29] are probably associated with the reorganization energies of the protein modes[30,31] that are active in the vibrational coherence. The protein structure would then be directly responsible for the very high quantum efficiency[17,27] of the charge-separation reactions in the reaction center.

A different sort of protein-derived structural origin for the vibrational coherence in the photosynthetic reaction center is suggested by the results from recent studies in our laboratory of the ground-state vibrational coherence observed in solutions of BChl. By far, the strongest contributions to the vibrational coherence arise from localized intermolecular modes with clustered, first-shell solvent molecules.[32–34] The pump−probe signals observed with *Q*-band excitation of BChl in polar solvents are modulated by rapidly damped (effective damping

* Corresponding author. E-mail: beckw@msu.edu. Fax: 517-353-1793.
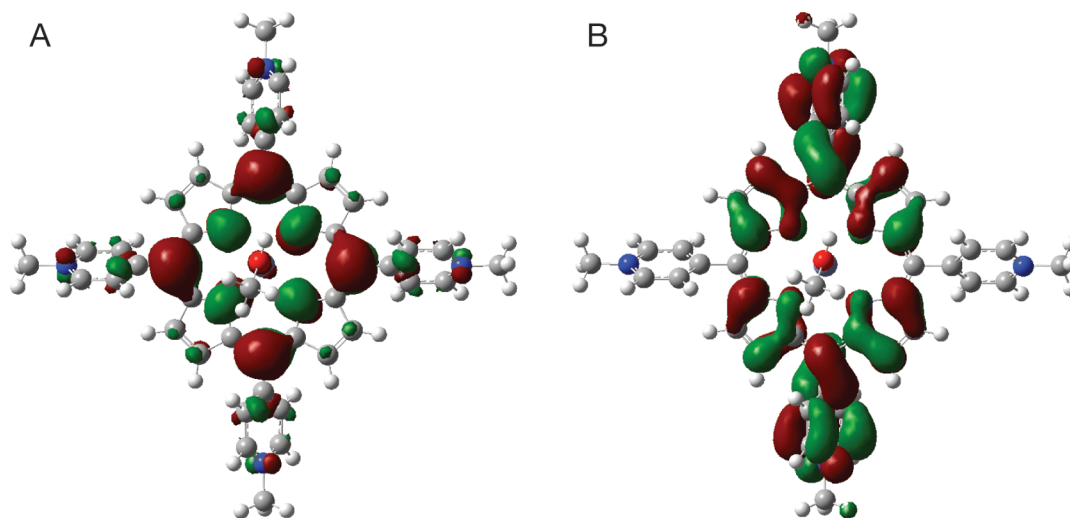† Current address: Department of Chemistry, Colorado State University, Fort Collins, Colorado 80523, United States.

A

B

Figure 1. Optimized structure of ZnTMPyP complexed with a single methanol molecule as an axial ligand to the Zn^{II} ion. The structure was obtained from an electronic structure calculation with Gaussian 03[36] using the B3LYP hybrid density functional at the 6-31G level of theory. The ball-and-stick structures are shown superimposed with density surfaces for (a) the highest occupied molecular orbital (HOMO) and for (b) the lowest unoccupied molecular orbital (LUMO). (From ref 35.)

time $\gamma < 200$ fs) components that shift to higher frequencies as the dipole moment of the solvent increases. The mean frequency of these modulation components follows the general trend expected for the natural frequency of a van der Waals intermolecular potential that includes dominant contributions from the London-dispersion and dipole−dipole interactions.[33] The slowly damped ($\gamma \geq 2000$ fs) modulation components that arise from the skeletal modes of the BChl macrocycle are perhaps 10 times less intense than those from the solvent modes.[32]

In our most recent contribution in this area, we reported our observations of intermolecular vibrational coherence in polar solutions of Zn^{II} *meso*-tetrakis(*N*-methylpyridyl)porphyrin (ZnTMPyP) with Soret-band (420-nm) excitation.[35] The normal modes of the porphyrin macrocycle and its single solvent-derived axial ligand contribute very slowly damped features to the vibrational coherence, some of which persist even to the 20-ps delay point. The rapidly damped, solvent-dependent modes again account for the dominant features. The dependence of the mean frequency of the rapidly damped components is consistent with an intermolecular potential that exhibits a lower mode frequency in the nonpolar limit than observed in BChl (70 cm^{-1} and 120 cm^{-1}, respectively), and an isotope-dependent shift was observed when the signals from methanol and perdeuterated methanol were compared. The magnitude of the shift indicates that the intermolecular modes arise in methanol solution predominantly from 1:1 complexes with the porphyrin solute.

The intermolecular potential we used in the discussion of the ground-state vibrational coherence in BChl and ZnTMPyP solutions includes only the terms that arise from the polarizability and dipole moment of the neutral solute and solvent. In ZnTMPyP, the π-electron density in the ground state is confined to the porphyrin macrocycle (see Figure 1a), so an attacking solvent molecule does not strongly sense the positive charges on the peripheral *N*-methylpyridyl rings. In the π^* excited states (see Figure 1b), however, the π-electron density is extensively delocalized from the porphyrin over two of the *N*-methylpyridyl rings, so the intermolecular potential between ZnTMPyP and clustered solvents should gain ion−dipole and ion−induced-dipole terms. These charge-dependent terms would be expected to contribute to a significant shift to higher frequency for the

intermolecular oscillator. We have put these ideas to the test in this contribution. We show that pump−probe signals obtained with Q-band (S_1 state) excitation of ZnTMPyP detect excited-state wavepacket motions that modulate a net excited-state absorption signal. As expected, the rapidly damped portion of the vibrational coherence shifts to a much higher frequency than observed in the ground-state vibrational coherence observed with Soret-band excitation. These results advance the hypothesis that intermolecular modes with first-solvation-shell components contribute dominantly to the low-frequency vibrational coherence in porphyrin and BChl systems. We conclude with a brief discussion of how the charge-dependent terms in the intermolecular potential should play an important dynamical role in the photosynthetic reaction center by enhancing the quantum efficiency of the charge-separation reactions.

2. Experimental Section

Sample Preparation. ZnTMPyP (CAS 28850-44-4) was used as received from Frontier Scientific. Methanol (CH$_3$OH, spectrophotometric grade) was obtained from Sigma-Aldrich. For use in femtosecond pump−probe experiments, solutions of ZnTMPyP were prepared by dissolving the dry ZnTMPyP powder in methanol to obtain an absorbance of 0.4 for a path length of 1.0 mm at the center of the laser spectrum at 625 nm, as detailed below. The solution was passed through a 0.22-μm filter prior to checking the absorbance. The samples were held in the femtosecond pump−probe spectrometer at room temperature (23 °C) in a fused-silica flow cuvette (0.5-mm path length). A peristaltic pump was used to circulate a 10-mL reservoir of sample solution through the cuvette at 2.70 mL/min. A fresh sample was prepared for each day's work, and the acquired signals were stored on a scan-by-scan basis so that any changes due to accumulated photochemistry during a given sample's exposure to laser excitation could be noted. The sample's absorption spectrum was monitored during each experiment for changes arising from photochemistry or permanent photobleaching.

Continuous-Wave Absorption and Fluorescence Spectroscopy. Absorption spectra were obtained at 23 °C with a Hitachi U-2000 spectrophotometer (2-nm bandpass). Fluorescence spectra were acquired at 23 °C with a Hitachi F-4500 spectro-

Vibrational Coherence in Methanol Solution of ZnTMPyP

J. Phys. Chem. B, Vol. 114, No. 46, 2010 **15271**

fluorimeter (5-nm bandpass for the excitation and emission monochromators). As presented as a function of wavenumber, the fluorescence intensities are multiplied by the square of the wavelength in order to compensate for the fixed (in wavelength units) spectral bandpass of the emission spectrometer.[37]

Femtosecond Spectroscopy. Femtosecond pump–probe transients with impulsive excitation were recorded using the dynamic-absorption technique, in which the probe beam is dispersed in a grating monochromator after passing through the sample.[1,4,8,9,38] Most of the instrumentation and methodology is similar to that described in our previous work on ZnTMPyP solutions with Soret-band excitation.[35] In this work, however, the pump and probe pulses were obtained from an optical parametric amplifier (Coherent OPA 9450), which was pumped by an amplified Ti:sapphire laser (Coherent Mira-SEED oscillator and a Coherent RegA 9050 regenerative amplifier, with Coherent Verdi V5 and V10 pump lasers, respectively). The laser was operated at a repetition rate of 250 kHz. The experiments were conducted with 13-nJ, 45-fs pump and 7.2-nJ probe pulses centered at 625 nm (15 nm fwhm, as measured with an Ocean Optics USB-2000 spectrometer/CCD detector with a 0.5-nm bandpass).

The pump and probe pulses were corrected for group-delay dispersion on the way to the sample by a SF10 Brewster prism-pair pulse compressor. The pump–probe time delay was scanned using a rapid-scanning delay stage (Clark-MXR, ODL-150) in a modified Mach–Zehnder interferometer with confocal sample and autocorrelation-crystal positions. Calcite polarizers and $\lambda/2$-retarding wave plates in the pump and probe beams set their planes of polarization at 90°; after passing through the sample, the probe beam was analyzed by another calcite polarizer oriented 90° relative to the pump-beam's plane of polarization, and then it was passed through a monochromator (Spex 270M, 4-nm bandpass) and detected by an amplified photodiode (Thorlabs PDA55). The monochromator's slits were adjusted to obtain a fairly narrow bandpass (4 nm) compared to the width of the laser's spectrum; the monochromator's grating was detuned from the laser's intensity maximum to the ~50% intensity point. This approach is similar to that used by Champion and co-workers in their studies of low-frequency vibrational coherence in heme proteins.[13–15] The pump–probe signal was obtained from the photodiode signal using a lock-in amplifier (Femto LIA-MV-200-H); the pump beam was modulated at 50 kHz by a $\lambda/4$-retarding photoelastic modulator (Hinds Instrumentation) with $\lambda/4$-retarding and $\lambda/2$-retarding waveplates and a calcite polarizer in series.

3. Results

Figure 2 shows continuous-wave absorption and fluorescence spectra from ZnTMPyP in methanol at 23 °C. The spectra are plotted as relative dipole strengths[37,39,40] as a function of wavenumber ν, $A(\nu)/\nu$ and $F(\nu)/\nu^3$ respectively. The fluorescence spectrum extends to the red from the 0–0 peak of the Q band, the absorption feature that corresponds to the transition from the ground state (S_0) to the first excited singlet state (S_1). Also shown in Figure 2 is the output spectrum from the OPA as it was tuned to 625 nm for the dynamic-absorption experiments. Because we wanted to detect vibrational coherence arising from coherent wavepacket motion on the S_1 state's potential-energy surface, the OPA was tuned as far to the red in the Q band as possible so that the stimulated-emission (SE) signal detected by the probe bandpass would be larger than the ground-state depletion signal. As estimated from the dipole-
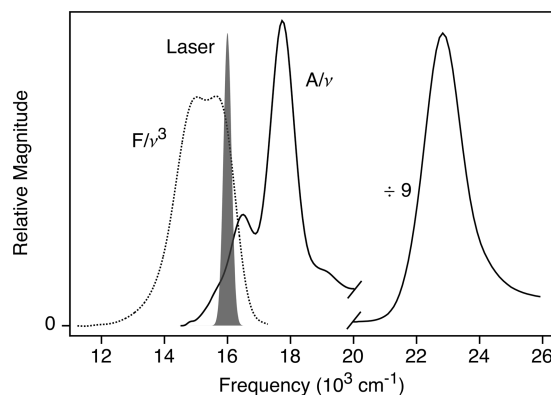

Figure 2. Soret ($\nu > 20000$ cm^{-1}) and Q-band region of the continuous-wave absorption (solid curve) and fluorescence (dotted curve) spectra from ZnTMPyP in methanol at room temperature (23 °C), plotted as the dipole strength, $A(\nu)/\nu$ and $F(\nu)/\nu^3$, respectively, and normalized to unit area for the fluorescence spectrum and Q-band. Superimposed with arbitrary scaling is the intensity spectrum of the 625-nm, 45-fs pulses used in the pump–probe experiment.
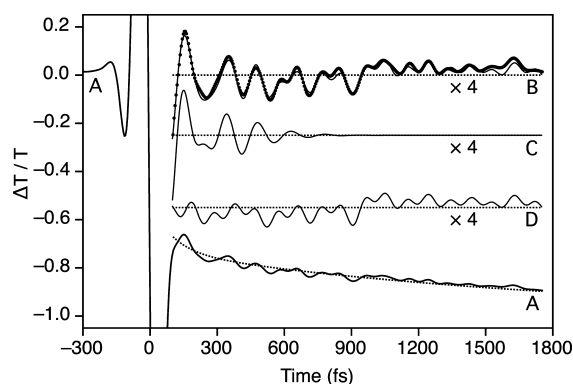

Figure 3. Femtosecond pump–probe dynamic absorption transient from ZnTMPyP in methanol and fitted rapidly and slowly damped oscillatory model components. The transient was obtained with 45-fs, 625-nm pump and probe pulses (see Figure 2) and detected with a 4-nm bandpass of the transmitted probe spectrum centered at 632 nm. (a) The pump-induced change in transmission signal ($\Delta T/T$) is shown superimposed on a biexponential function (dashed curve) fitted over the 100-fs to 3.5-ps range of the form $A_0(A_1 e^{-t/\tau_1} + A_2 e^{-t/\tau_2} - 1)$, with $A_0 = 3.00 \times 10^{-3}$, $A_1 = 0.204$, $\tau_1 = 98$ fs, $A_2 = 0.272$, and $\tau_2 = 1.8$ ps. As plotted, the signal is normalized by dividing by the nondecaying fraction, A_0. (b) Oscillatory residual, obtained by subtracting the biexponential function from the pump–probe transient. The data points are superimposed on a model containing both slowly and rapidly damped oscillatory components. The model parameters are listed in Tables 1 and 2. (c) Rapidly damped ($\Delta\omega > 10$ cm^{-1}) part of the fitted model (see Table 2). (d) Slowly damped ($\Delta\omega < 10$ cm^{-1}) part of the fitted model (see Table 1). Traces b–d are shown with a ×4 expanded ordinate compared to that for trace a, and the zero levels for each are marked by a dashed line.

strength spectra, at the 632-nm center of the probe bandpass the SE signal is 5 times larger than the photobleaching (PB) signal.

The dynamic-absorption transient obtained from ZnTMPyP in methanol under these experimental conditions is shown in Figure 3a. The plotted signal is the average of that accumulated over several days of data acquisition. Following an intense bipolar spike that goes off the plotted scale near the pump–probe zero-delay point,[41–43] the transient exhibits a pattern of cosinusoidal modulations superimposed on a rising transient of net excited-state absorption (ESA) character. In order to isolate the oscillatory portion, we fit a biexponential background function to the signal over the 100-fs–3.5-ps range, where the signal

TABLE 1: Gaussian Lineshape Parameters for the Slowly Damped Modulation Components Obtained from the 625-nm Pump−Probe Transient from ZnTMPyP in Methanol[a]

component	ω_0 (cm^{-1})	$\Delta\omega$ (cm^{-1})	amplitude[b]
1	15	2.55	2.84
2	37	2.36	1.00
3	63	2.35	0.507
4	94	9.41	0.776
5	112	9.41	0.761
6	157	2.77	1.42
7	172	2.35	0.597
8	195	4.61	0.597
9	216	2.35	0.313
10	255	2.35	0.373
11	313	4.66	0.358
12	346	9.04	2.54

[a] See Figure 3. [b] Normalized relative to component 2, which has an amplitude of 6.72×10^{-3} relative to the fitted nondecaying fraction, A_0 (see Figure 3).

TABLE 2: Gaussian Lineshape Parameters and Effective Exponential Damping Times for the Rapidly Damped Modulation Components Obtained from the 625-nm Pump−Probe Transient of ZnTMPyP in Methanol[a]

component	ω_0 (cm^{-1})	$\Delta\omega$ (cm^{-1})	γ (fs)[b]	amplitude[c]
1	220	44.0	309	17.9
2	285	70.8	193	22.4

[a] See Figure 3. [b] Damping time of best-fit exponentially damped cosinusoid (see eq 4). [c] Normalized relative to the 37-cm^{-1} slowly damped component (see Table 1).

appears to have leveled off. The fit parameters for the background function are listed in the caption to Figure 3. The oscillatory part of the signal was obtained as the difference between the signal and the biexponential background. As plotted in an expanded view in Figure 3b, it consists of a very rapidly damped portion over the 100−800-fs range followed by a more slowly damped part that persists at least to the 2000-fs range. This character is similar to that observed in polar solutions of BChl and in polar solutions of ZnTMPyP with Soret-band excitation.[33,35] Because the background function is monotonic (the two exponentials have amplitudes of the same sign), its subtraction does not introduce any oscillatory components into the residual.

The oscillatory residual is superimposed in Figure 3b on a model composed of slowly and rapidly damped oscillatory components. The modeled region was confined to the >100-fs portion to avoid modeling of the spike near time zero,[43] and it extends out to 1.8 ps, at which point the signal/noise ratio has degraded. The model function consists of a sum of damped cosinusoids of the form

$$I_i(t) = A_i e^{-t^2\sigma_i^2/2} \cos(\omega_{0i}t - \phi_i)/\sqrt{2\pi} \tag{1}$$

with each component i having a center frequency ω_{0i} and phase ϕ_i. These waveforms correspond to Gaussian line shapes in the frequency domain

$$I_i(\omega) = A_i e^{-(\omega - \omega_{0i})^2/(2\sigma_i^2)}/(\sigma_i\sqrt{2\pi}) \tag{2}$$

where the line width is controlled by the standard deviation, $\sigma_i = \Delta\omega_i/2(2 \ln 2)^{1/2}$, with $\Delta\omega_i$ representing the full width at half-maximum. Equations 1 and 2 are normalized so that the
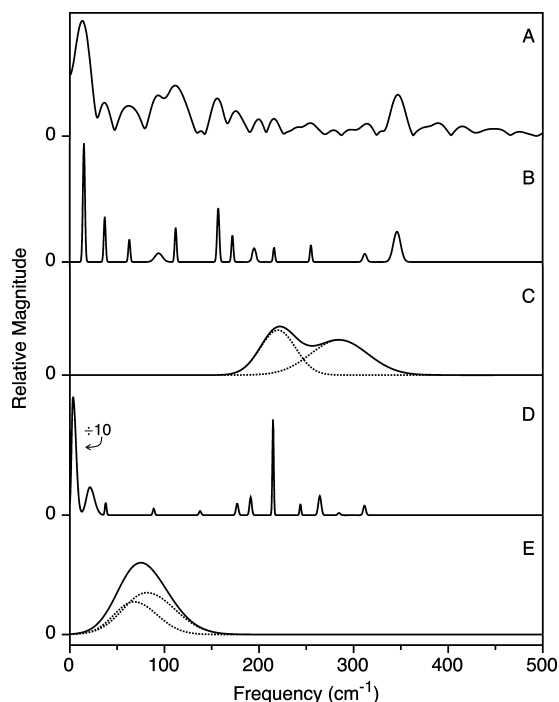

Figure 4. Comparison of the intensities and lineshapes observed in the excited-state and ground-state vibrational coherence from ZnTMPyP in methanol. *Excited state*, from the 625-nm pump−probe signal, see Figure 3: (a) Hanning-windowed, Fourier-transform magnitude spectrum; Spectra for (b) the slowly damped ($\Delta\omega < 10$ cm^{-1}) and (c) the rapidly damped ($\Delta\omega > 10$ cm^{-1}) components from the time-domain model. *Ground state*, from the 420-nm pump−probe signal, from ref 35: spectra for (d) the slowly damped ($\Delta\omega < 10$ cm^{-1}) and (e) the rapidly damped ($\Delta\omega > 10$ cm^{-1}) components from the time-domain model. In c and e, the sum of the two rapidly damped components (dotted lines) is shown as the solid trace. The scaling factor for d and e is 1.6 times smaller than that for b and c.

amplitude A_i corresponds to the area of the line shape in the frequency domain and to the intensity of the signal in the time domain. Except as noted in the following, the fitting procedure was as described in detail in the paper on the ground-state vibrational coherence from ZnTMPyP.[35]

Starting parameters for the model for the slowly damped components ($\Delta\omega < 10$ cm^{-1}) were obtained from a Hanning-windowed Fourier-transform spectrum (see Figure 4a). The Hanning window function[44]

$$w(k) = 0.5\left[1 - \cos\left(\frac{2\pi k}{n + 1}\right)\right] \tag{3}$$

is defined for the data point index k in terms of the number of data points in the segment n; its product with the oscillatory residual suppresses the rapidly damped portion of the signal and applies linebroadening to the slowly damped components by gradually forcing the intensity at the beginning ($t = 100$ fs) and end ($t = 1.8$ ps) to zero amplitude. The 12 most intense peaks in the Fourier-transform spectrum were included in the model. The fit parameters for these slowly damped components are listed in Table 1, and their time-domain sum is shown as Figure 3d.

The remaining, rapidly damped ($\Delta\omega > 10$ cm^{-1}) part of the oscillatory residual was then modeled as the sum of two broad Gaussian components. The fit was not improved by inclusion in the line shape of an asymmetry or skew parameter, as was previously required in the modeling of the rapidly damped

components observed in the ground state.[35] The two components are assigned, in order of frequency, to the hindered translational and librational intermolecular modes between the porphyrin macrocycle and its clustered, first-solvation-shell solvent molecules.[33,35] This assignment is made in analogy to the ordering of the intermolecular mode frequencies that is inferred from instantaneous normal-mode spectra in polar solution.[45,46] The fit parameters for these components are listed in Table 2; the time-domain sum of the two components is plotted as Figure 3c. Also included in Table 2 are effective damping times γ for a best-fit exponentially damped cosinusoid of the form

$$I_i(t) = A_i e^{-t/\gamma_i} \cos(\omega_{0i} t - \phi_i) \qquad (4)$$

which corresponds in the frequency domain to a Lorentzian line shape. The tabulated values of γ were obtained as previously described by fitting each Gaussian component in the model individually to eq 4. This procedure provides a rough estimate of the lower limit for the damping time.[35]

Figure 4b,c shows frequency domain representations of the slowly and rapidly damped portions of the optimized model. These spectra should be compared to Figure 4d,e, which shows the spectra for the slowly and rapidly damped components in the ground-state vibrational coherence.[35] The rapidly damped components in Figure 4c are clearly shifted to a much higher frequency from those in Figure 4e. From the sum of the two underlining component lineshapes (see Figure 4c,e), $\mathcal{M}(\omega) = I_1(\omega) + I_2(\omega)$, the mean frequency was obtained using a normalized mean-value relation:

$$\langle \omega \rangle = \frac{\int_0^\infty d\omega \, \mathcal{M}(\omega)\omega}{\int_0^\infty d\omega \, \mathcal{M}(\omega)} \qquad (5)$$

The mean frequency of the sum of the two rapidly damped components shown in Figure 4c is 256 cm^{-1}, whereas the mean frequency for those in Figure 4e is 79 cm^{-1}.

4. Discussion

The pump−probe signal from ZnTMPyP with Q-band excitation at 625 nm is modulated by coherent wavepacket motions on the first excited-state (S_1) potential-energy surface. This assignment is based primarily on the tuning of the laser spectrum, the choice of the detected probe bandwidth (see Figure 2), and the observation of a rising net ESA signal that persists to the end of the recording. The net ESA character is consistent with the results of Fontaine-Aupart and co-workers,[47] who noted a long-lived ESA signal at probe wavelengths above 575 nm in their pump−continuum−probe time-resolved spectra. In our experiments, the OPA was tuned so that the red side of the output spectrum, from which the probe bandpass was selected, overlaps favorably with the SE spectrum (see Figure 2). Owing to the 5:1 SE:PB ratio, as judged from the ratio of the continuous-wave fluorescence and absorption dipole strengths centered at the detected probe bandpass, respectively, and because of the net ESA character (the strength of the ESA part of the signal is larger than of the sum of the photobleaching and SE parts), we estimate that ground-state wavepacket motions make less than a 10% contribution to the pump−probe signal. The SE and ESA signals are synchronously modulated by the S_1-state wavepacket.

The frequency dependence of the modulation intensities for the slowly damped ($\gamma > 1.5$ ps, $\Delta\omega < 10$ cm^{-1}) components observed in Figure 4a,b is also consistent with an assignment to excited-state coherent wavepacket motions. In systems where the ground- and excited-state potential-energy surfaces are displaced with respect to the coordinate of the vibrational mode, wavepackets on the ground- and excited-state potential surfaces are set in motion by two successive actions of the pump field.[2–4,48] The ground-state wavepacket is created by a process that directly corresponds to resonance Raman scattering. The pump−probe signal is modulated optimally by ground-state wavepacket motion when the pump-pulse duration is about one-third of the mode's period.[3] As we explained previously, the $\sim$222 cm^{-1} maximum observed in the intensity profile of the slowly damped features detected with Soret-band excitation (see Figure 4d) is consistent with an assignment to ground-state wavepacket motions because of our use of 50-fs pump pulses in that experiment.[35] In contrast, for excited-state wavepacket motion, the amplitudes are expected to increase monotonically as the frequency decreases.[3] The intensities in Figure 4b exhibit the expected trend. The main exception is the relatively intense 346-cm^{-1} peak, which we assign to an out-of-plane deformation mode localized on the N-methylpyridyl rings based on assignments of peaks at similar frequencies in continuous-wave resonance Raman spectra of ZnTMPyP and other N-methylpyridyl porphyrins.[49] The 3-cm^{-1} component we observed in the ground-state vibrational coherence with Soret-band excitation (Figure 4d) with recordings out to 25 ps, more than twice the vibrational period, cannot be detected in the Q-band signal (Figure 4b) because the range of the recording extends only to 3.5 ps. This component was assigned previously to internal rotation of the N-methylpyridyl rings with respect to the porphyrin.[35]

Except for the 3-cm^{-1} and 346-cm^{-1} peaks discussed above, the frequencies of the components observed in the slowly damped excited-state vibrational coherence (Figure 4b) are within 1 cm^{-1} of those observed in the ground-state vibrational coherence signal (Figure 4d). As discussed previously,[35] the normal-mode analysis based on the electronic structure calculation used in Figure 1 shows that most of these modes arise from out-of-plane deformations of the porphyrin macrocycle. The 37-cm^{-1} and 216-cm^{-1} components are assigned to the metal-doming and Zn^{II}−axial-ligand stretching modes, respectively. Somewhat higher frequencies for these modes have been reported for Fe^{II} porphyrins.[50]

The rapidly damped ($\gamma < 400$ fs, $\Delta\omega > 15$ cm^{-1}) features shown in Figure 4d,e correspond to the intermolecular modes between the ZnTMPyP molecule and first-shell solvent molecules. We assign these features to wavepacket motions on the excited-state potential surface because of the laser tuning, as argued above, but this assignment seems warranted also because the mean frequency (256 cm^{-1}) is markedly different from that observed previously for the ground-state motions obtained with Soret-band excitation (79 cm^{-1}). The increased frequency for the excited-state wavepacket motions is explained by the activation of solute-charge-dependent terms in the van der Waals intermolecular potential. In the ground state of ZnTMPyP, because the π-electron density is confined to the porphyrin ring (see Figure 1) and the porphyrin is effectively neutral, the intermolecular potential can be expressed as

$$V_0(r) = a/r^{12} - \left(b\alpha_1\alpha_2 + \frac{c|\boldsymbol{\mu}_1|^2|\boldsymbol{\mu}_2|^2}{(4\pi\varepsilon_0)^2} + \frac{\alpha_2|\boldsymbol{\mu}_1|^2 + \alpha_1|\boldsymbol{\mu}_2|^2}{4\pi\varepsilon_0} \right)/D^2 r^6 \quad (6)$$

As shown previously,[33] a Taylor-series expansion of eq 6 around the equilibrium geometry gives an expression for the natural frequency of the intermolecular mode:

$$\nu = \frac{3}{(2a)^{2/3}} \left(b\alpha_1\alpha_2 + \frac{c|\boldsymbol{\mu}_1|^2|\boldsymbol{\mu}_2|^2}{(4\pi\varepsilon_0)^2} + \frac{\alpha_2|\boldsymbol{\mu}_1|^2 + \alpha_1|\boldsymbol{\mu}_2|^2}{4\pi\varepsilon_0} \right)^{7/6} /2\pi D^{7/3}\mu^{1/2} \quad (7)$$

In these equations, $\boldsymbol{\mu}_i$ and α_i correspond to the dipole moment and polarizability for the solute (subscript 1) and solvent (subscript 2), r is the distance between the two molecules, μ is the reduced mass for the intermolecular oscillator, D represents the dielectric constant for the solvent, and ε_0 relates the permittivity of free space; the constant a scales the Pauli exchange interaction, b scales the London-dispersion interaction, $c = 2/3k_BT$ scales the dipole–dipole interactions, and the $\alpha_2|\boldsymbol{\mu}_1|^2$ and $\alpha_1|\boldsymbol{\mu}_2|^2$ terms correspond to dipole–induced-dipole interactions (see Table 3).[51–54] As expressed above, the dipole-dependent terms apply to the high-temperature limit, where k_BT is much greater than the well depth, so the interaction is averaged over all relative orientations.[53]

In the excited state, the π-electron density is extensively delocalized from the porphyrin region to two of the N-methylpyridyl rings (see Figure 1), so the formal charges on the rings are also delocalized. As noted previously,[35] the intermolecular potential now should include two additional solute-charge-dependent terms corresponding to the ion–dipole and ion–induced-dipole interactions with the charge Q:

$$V_Q(r) = V_0 - \left(\frac{cQ|\boldsymbol{\mu}_2|^2}{(4\pi\varepsilon_0)^2} + \frac{\alpha_2 Q^2}{4\pi\varepsilon_0} \right)/2D^2 r^4 \quad (8)$$

Both of the new terms are attractive: the ion–dipole term depends linearly on the charge Q of the solute and on the square of the solvent's dipole moment, $\boldsymbol{\mu}_2$, and the ion–induced-dipole term contains the polarizability α_2 of the solvent and the square of the charge, Q^2. Both terms are scaled by r^{-4}, so the charged potential V_Q reaches much larger intermolecular distances than does the neutral potential V_0 (eq 6). The relation for the natural mode frequency that follows from a Taylor-series expansion of V_Q around the equilibrium geometry is not shown here owing to its length. It predicts that the mode frequency should significantly increase over that predicted by eq 7 for V_0.

Figure 5 shows three model curves for the ZnTMPyP–CH₃OH intermolecular potential to illustrate how the solute-charge-dependent terms substantially stabilize the equilibrium structure. Most of the parameters in V_0 and V_Q (eqs 6 and 8) are obtained from the literature (see Table 3). The coefficient for the exchange interaction, a, can be estimated given the experimental measurement of the ground-state mode frequency (79 cm⁻¹) and an assumption that $Q = 0$ in the ground state, so that the charge-dependent terms do not contribute to the intermolecular potential. In the excited state, the π-electron density extends over two of the N-methylpy-

TABLE 3: Parameters for ZnTMPyP–CH₃OH Intermolecular Potentials at 298 K[a]

parameters[b]	symbol	value
exchange (Pauli) interaction coefficient	a	76.2 eV Å¹²
London-dispersion interaction coefficient	b	9.35 eV[c,d]
ZnTMPyP dipole moment	$|\boldsymbol{\mu}_1|$	0.663 D[c]
CH₃OH dipole moment	$|\boldsymbol{\mu}_2|$	1.70 D[d]
ZnTMPyP polarizability	α_1	109.8 Å³ [c]
CH₃OH polarizability	α_2	3.29 Å³ [d]
CH₃OH dielectric constant	D	33[d]
equilibrium geometry with $Q = 0$	r_{eq}	1.90 Å
	V_{eq}	286 cm⁻¹
equilibrium geometry with $Q = 1$	r_{eq}	1.83 Å
	V_{eq}	510 cm⁻¹
equilibrium geometry with $Q = 2$	r_{eq}	1.72 Å
	V_{eq}	1336 cm⁻¹

[a] See Figure 5. [b] See eqs 6–8 and the text. [c] From B3LYP/6-31G calculation (see ref 35). [d] From ref 55.
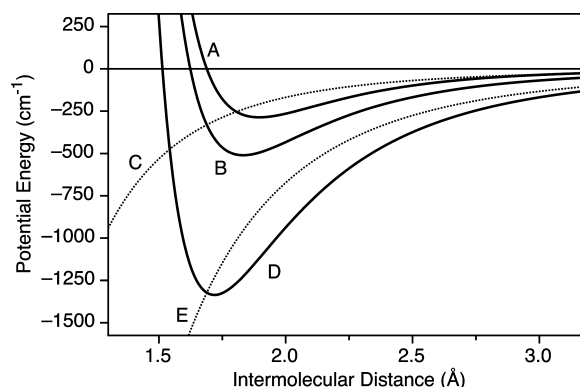

Figure 5. Model potential-energy curves at 298 K for the ZnTMPyP–CH₃OH complex as a function of the charge Q on the ZnTMPyP moiety: (a) $Q = 0$; (b) $Q = 1$; (c) the attractive, charge-dependent terms for $Q = 1$; (d) $Q = 2$; and (e) the attractive, charge-dependent terms for $Q = 2$. The curves were calculated using eq 7 and the experimentally observed ground-state intermolecular mode frequency, 79 cm⁻¹ (see ref 35). Table 3 lists the parameters and compares r_{eq} and V_{eq} for curves a, b, and d.

ridyl rings, so it is reasonable to suppose that two charges are introduced. As Q increases from 0 to 2, the potential-well depth V_{eq} is 168 cm⁻¹, which is about two-thirds of the mean frequency determined from the rapidly damped components shown in Figure 4c, 256 cm⁻¹. Note that the assumption of orientational averaging made above is probably not even valid for the ground state given the calculated well depths. A better prediction of the excited-state mode frequency might be obtained from an improved potential that explicitly includes the excited-state charge distribution and employs a molecular dynamics simulation to project a proper distribution of solvent–solute interaction distances and orientations.

Conclusions

The finding that the frequency of the ZnTMPyP–methanol intermolecular mode is larger in the S₁ state than in the ground state (S₀) supports the suggestions made in the Introduction about the nature of the coupling of the solvent molecules to the π–π* transition and about the importance of charge-dependent terms in the intermolecular potential. The relatively low mode

Vibrational Coherence in Methanol Solution of ZnTMPyP
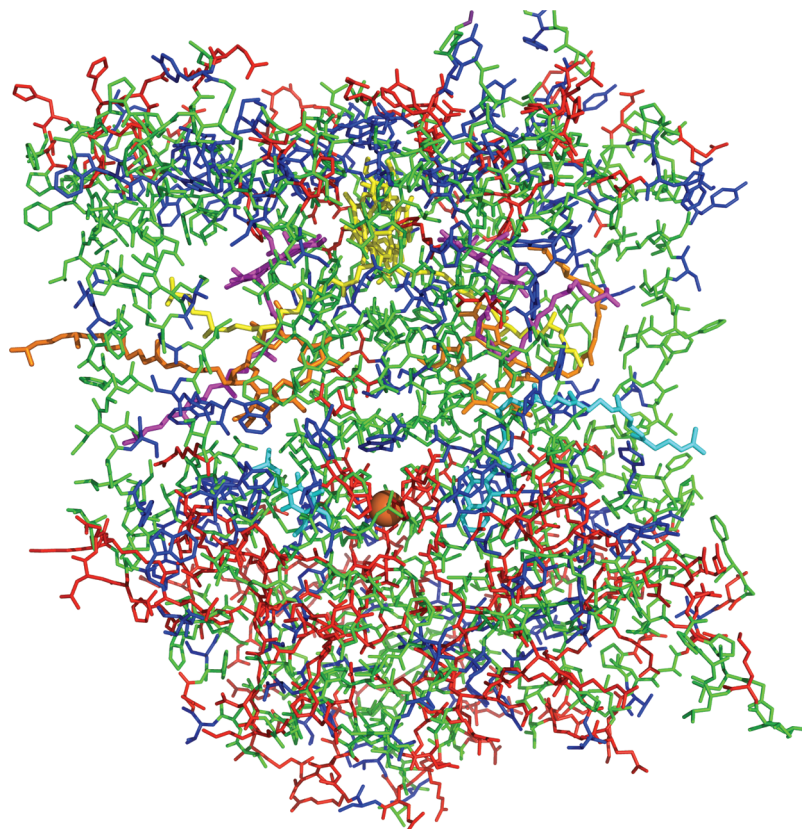
J. Phys. Chem. B, Vol. 114, No. 46, 2010 **15275**

Figure 6. Structure of the photosynthetic reaction center from *Blastochloris viridis*, as rendered from the pdb file 1PRC.[26,27] The bacteriochlorophyll (yellow and magenta), bacteriopheophytin (orange), and quinone (cyan) cofactors are rendered as thick stick figures; amino acids with polar (blue), charged (red), and nonpolar (green) side chains are rendered as thin stick figures. The cytochrome subunit is not shown. The structure is oriented so that the active electron-transfer branch of chromophores is to the right of the vertical axis between the primary electron donor P (yellow) and the nonheme Fe atom (red sphere).

frequency observed in the ground-state vibrational coherence is consistent with an effective absence of the charge-dependent terms in the ground-state potential, which indicates that the intermolecular wavepacket motions detected in the dynamic-absorption experiment involve solvent molecules that make a direct attack on the π-electron density localized on the porphyrin macrocycle. In the excited state, the increased intermolecular mode frequency is consistent with activation of the charge-dependent terms in the excited-state potential owing to extensive delocalization of the π-electron density from the porphyrin to the *N*-methylpyridyl rings (see Figure 1). The excited-state and ground-state wavepacket motions are launched by the resulting change of the intermolecular potential's depth and displacement.

These conclusions suggest an important dynamical role for the intermolecular modes between the redox chromophores and the surrounding protein medium in photosynthetic reaction centers. In general, the forward, charge-separation reactions involve a downhill potential-energy-surface crossing from a neutral chromophore's reactant surface to a charged chromophore's product surface, whereas the reverse, charge-recombination reactions involve an uphill crossing from the charged chromophore's surface back to the neutral chromophore's surface. As depicted in Figure 6, the primary electron-donor P and the acceptor quinones Q_A and Q_B are adjacent to charged (red) or polar (blue) solvation partners in the peripheral regions of the structure, so the charged products P^+, Q_A^-, and Q_B^- of the primary and secondary charge-separation reactions, respectively, can be rapidly trapped by short-ranged exothermic displacements of the intermolecular modes. In contrast, the bacteriopheophytin

acceptor $BPhe_L$ is located in a nonpolar (green) region of the transmembrane protein structure.[26–28] This positioning affords the system an important dynamical advantage: it is removed enough from polar or charged groups that the $BPhe_L^-$ radical anion product of the primary charge separation is not too deeply stabilized by its neighboring solvation partners. If there were any charges or dipoles in its neighborhood, the activation energy for the secondary charge-separation reaction that shuttles the negative charge from $BPhe_L^-$ to the Q_A acceptor would be increased; the crossing from the charged chromophore's reactant surface to the corresponding neutral chromophore's product surface is uphill, so any nearby charges or dipoles would slow the rate and make the reverse, charge-recombination reaction more competitive in rate. Thus, the quantum efficiency of the solar energy conversion process in the photosynthetic reaction center is clearly enhanced by the intermolecular modes with the surrounding protein structure without requiring long-range motions or a reorganization of the protein structure.

The protein-derived medium for the electron-transfer reactions of the photosynthetic reaction center affords the additional advantage of highly ordering the solvation partners around the redox chromophores so that the interactions and the associated dynamics can be specifically tuned by the structure. Compared to the inhomogeneously broadened line shape[32,33] observed from the disordered environment provided by the first-shell solvent molecules in a polar liquid, the ordered intermolecular modes between a BChl macrocycle in the reaction center and a polar group from the surrounding protein would present a narrow line shape that might be comparable in breadth to that from one of

the BChl's intramolecular, skeletal vibrational modes.[34] From that part of the first solvation shell that is occupied by a nonpolar group, however, the intermolecular modes would be primarily governed by the London-dispersion term in the intermolecular potential, which depends only on the polarizability.[33,35] This part of the interaction would contribute a broad, inhomogeneously broadened line shape on which the sharper, dipolar features are superimposed. This picture accounts for several aspects of the spectra from the vibrational coherence observed in wild-type and mutant reaction centers.[24] An important test of this hypothesis might be made in a single BChl or porphyrin-containing protein by perturbing the overall folded structure so that the distances between the chromophore and its solvation partners are varied.

References and Notes

(1) Fragnito, H. L.; Bigot, J.-Y.; Becker, P. C.; Shank, C. V. Evolution of the vibronic absorption spectrum in a molecule following impulsive excitation with a 6-fs optical pulse. *Chem. Phys. Lett.* **1989**, *160*, 101–104.

(2) Pollard, W. T.; Fragnito, H. L.; Bigot, J.-Y.; Shank, C. V.; Mathies, R. A. Quantum-mechanical theory for 6 fs dynamic absorption spectroscopy and its application to nile blue. *Chem. Phys. Lett.* **1990**, *168*, 239–245.

(3) Pollard, W. T.; Mathies, R. A. Analysis of femtosecond dynamic absorption spectra of nonstationary states. *Annu. Rev. Phys. Chem.* **1992**, *43*, 497–523.

(4) Pollard, W. T.; Dexheimer, S. L.; Wang, Q.; Peteanu, L. A.; Shank, C. V.; Mathies, R. A. Theory of dynamic absorption spectroscopy of nonstationary states. 4. Application to 12-fs resonant impulsive Raman spectroscopy of bacteriorhodopsin. *J. Phys. Chem.* **1992**, *96*, 6147–6158.

(5) Arnett, D. C.; Vohringer, P.; Scherer, N. F. Excitation dephasing, product formation, and vibrational coherence in an intervalence charge-transfer reaction. *J. Am. Chem. Soc.* **1995**, *117*, 12262–12272.

(6) Yang, T.-S.; Chang, M.-S.; Chang, R.; Hayashi, M.; Lin, S. H.; Vohringer, P.; Dietz, W.; Scherer, N. F. Femtosecond pump-probe study of molecular vibronic structures and dynamics of a cyanine dye in solution. *J. Chem. Phys.* **1999**, *110*, 12070–12081.

(7) Carson, E. A.; Diffey, W. M.; Shelly, K. R.; Lampa-Pastirk, S.; Dillman, K. L.; Schleicher, J. M.; Beck, W. F. Dynamic-absorption spectral contours: vibrational phase-dependent resolution of low-frequency coherent wave-packet motion of IR144 on the ground and excited $\pi-\pi^*$ surfaces. *J. Phys. Chem. A* **2004**, *108*, 1489–1500.

(8) Schoenlein, R. W.; Peteanu, L. A.; Mathies, R. A.; Shank, C. V. The first step in vision: Femtosecond isomerization of rhodopsin. *Science* **1991**, *254*, 412–415.

(9) Dexheimer, S. L.; Wang, Q.; Peteanu, L. A.; Pollard, W. T.; Mathies, R. A.; Shank, C. V. Femtosecond impulsive excitation of nonstationary vibrational states in bacteriorhodopsin. *Chem. Phys. Lett.* **1992**, *188*, 61–66.

(10) Peteanu, L. A.; Schoenlein, R. W.; Wang, Q.; Mathies, R. A.; Shank, C. V. The first step in vision occurs in femtoseconds: Complete blue and red spectral studies. *Proc. Natl. Acad. Sci. U.S.A.* **1993**, *90*, 11762–11766.

(11) Wang, Q.; Kochendoerfer, G. G.; Schoenlein, R. W.; Verdegem, P. J. E.; Lugtenburg, J.; Mathies, R. A.; Shank, C. V. Femtosecond spectroscopy of a 13-demethylrhodopsin visual pigment analogue: The role of nonbonded interactions in the isomerization process. *J. Phys. Chem.* **1996**, *100*, 17388–17394.

(12) Bardeen, C. J.; Wang, Q.; Shank, C. V. Femtosecond chirped pulse excitation of vibrational wave packets in LD690 and bacteriorhodopsin. *J. Phys. Chem. A* **1998**, *102*, 2759–2766.

(13) Zhu, L.; Li, P.; Huang, M.; Sage, J. T.; Champion, P. M. Real time observation of low frequency heme protein vibrations using femtosecond coherence spectroscopy. *Phys. Rev. Lett.* **1994**, *72*, 301–304.

(14) Wang, W.; Ye, X.; Demidov, A. A.; Rosca, F.; Sjodin, T.; Cao, W.; Sheeran, M.; Champion, P. M. Femtosecond multicolor pump-probe spectroscopy of ferrous cytochrome *c*. *J. Phys. Chem. B* **2000**, *104*, 10789–10801.

(15) Rosca, F.; Ionascu, D.; Kumar, A. T. N.; Demidov, A. A.; Champion, P. M. Femtosecond coherence spectroscopy using spectrally selective differential photodetection. *Chem. Phys. Lett.* **2001**, *337*, 107–116.

(16) Liebl, U.; Lipowski, G.; Negrerie, M.; Lambry, J.-C.; Martin, J.-L.; Vos, M. H. Coherent reaction dynamics in a bacterial cytochrome *c* oxidase. *Nature* **1999**, *401*, 181–184.

(17) Vos, M. H.; Lambry, J.-C.; Robles, S. J.; Youvan, D. C.; Breton, J.; Martin, J.-L. Direct observation of vibrational coherence in bacterial reaction centers using femtosecond absorption spectroscopy. *Proc. Natl. Acad. Sci. U.S.A.* **1991**, *88*, 8885–8889.

(18) Vos, M. H.; Lambry, J.-C.; Robles, S. J.; Youvan, D. C.; Breton, J.; Martin, J.-L. Femtosecond spectral evolution of the excited state of bacterial reaction centers at 10 K. *Proc. Natl. Acad. Sci. U.S.A.* **1992**, *89*, 613–617.

(19) Vos, M. H.; Rappaport, F.; Lambry, J.-C.; Breton, J.; Martin, J.-L. Visualization of the coherent nuclear motion in a membrane protein by femtosecond spectroscopy. *Nature* **1993**, *363*, 320–325.

(20) Vos, M. H.; Jones, M. R.; Hunter, C. N.; Breton, J.; Lambry, J.-C.; Martin, J.-L. Coherent dynamics during the primary electron-transfer reaction in membrane-bound reaction centers of *Rhodobacter sphaeroides*. *Biochemistry* **1994**, *33*, 6750–6757.

(21) Vos, M. H.; Jones, M. R.; McGlynn, P.; Hunter, C. N.; Breton, J.; Martin, J.-L. Influence of the membrane environment on vibrational motions in reaction centers of *Rhodobacter sphaeroides*. *Biochim. Biophys. Acta* **1994**, *1186*, 117–122.

(22) Vos, M. H.; Jones, M. R.; Breton, J.; Lambry, J.-C.; Martin, J.-L. Vibrational dephasing of long- and short-lived primary donor states in mutant reaction centers of *Rhodobacter sphaeroides*. *Biochemistry* **1996**, *35*, 2687–2692.

(23) Vos, M. H.; Jones, M. R.; Martin, J.-L. Vibrational coherence in bacterial reaction centers: Spectroscopic characterisation of motions active during primary electron transfer. *Chem. Phys.* **1998**, *233*, 179–190.

(24) Rischel, C.; Spiedel, D.; Ridge, J. P.; Jones, M. R.; Breton, J.; Lambry, J.-C.; Martin, J.-L.; Vos, M. H. Low frequency vibrational modes in proteins: changes induced by point-mutations in the protein-cofactor matrix of bacterial reaction centers. *Proc. Natl. Acad. Sci. U.S.A.* **1998**, *95*, 12306–12311.

(25) Vos, M. H.; Martin, J.-L. Femtosecond processes in proteins. *Biochim. Biophys. Acta* **1999**, *1411*, 1–20.

(26) Deisenhofer, J.; Epp, O.; Miki, K.; Huber, R.; Michel, H. X-ray structure analysis of a membrane protein complex: electron density map at 3 Å resolution and a model of the chromophores of the photosynthetic reaction center from *Rhodopseudomonas viridis*. *J. Mol. Biol.* **1984**, *180*, 385–398.

(27) Deisenhofer, J.; Epp, O.; Miki, K.; Huber, R.; Michel, H. Structure of the protein subunits in the photosynthetic reaction center of *Rhodopseudomonas viridis* at 3.1 Å resolution. *Nature* **1985**, *318*, 618–624.

(28) Deisenhofer, J.; Michel, H. The photosynthetic reaction center from the purple bacterium *Rhodopseudomonas viridis*. *Science* **1989**, *245*, 1463–1473.

(29) Fleming, G. R.; Martin, J.-L.; Breton, J. Rates of primary electron transfer in photosynthetic reaction centers and their mechanistic implications. *Nature* **1988**, *333*, 190–192.

(30) Bixon, M.; Jortner, J. Coupling of protein modes to electron transfer in bacterial photosynthesis. *J. Phys. Chem.* **1986**, *90*, 3795–3800.

(31) Bixon, M.; Jortner, J. Activationless and pseudoactivationless primary electron transfer in photosynthetic bacterial reaction centers. *Chem. Phys. Lett.* **1989**, *159*, 17–20.

(32) Shelly, K. R.; Carson, E. A.; Beck, W. F. Vibrational coherence from the dipyridine complex of bacteriochlorophyll *a*: Intramolecular modes in the $10-220$ cm^{-1} regime, intermolecular solvent modes, and relevance to photosynthesis. *J. Am. Chem. Soc.* **2003**, *125*, 11810–11811.

(33) Shelly, K. R.; Golovich, E. C.; Beck, W. F. Intermolecular vibrational coherence in bacteriochlorophyll *a* with clustered polar solvent molecules. *J. Phys. Chem. B* **2006**, *110*, 20586–20595.

(34) Shelly, K. R.; Golovich, E. C.; Dillman, K. L.; Beck, W. F. Intermolecular vibrational coherence in the purple-bacterial light-harvesting proteins B777 and B820 from *Rhodospirillum rubrum*. *J. Phys. Chem. B* **2008**, *112*, 1299–1307.

(35) Dillman, K. L.; Shelly, K. R.; Beck, W. F. Vibrational coherence in polar solutions of Zn^{II} tetrakis(*N*-methylpyridyl)porphyrin with Soret-band excitation: Rapidly damped intermolecular modes with clustered solvent molecules and slowly damped intramolecular modes from the porphyrin macrocycle. *J. Phys. Chem. B* **2009**, *113*, 6127–6139.

(36) Frisch, M. J.; Trucks, G. W.; Schlegel, H. B.; Scuseria, G. E.; Robb, M. A.; Cheeseman, J. R.; Montgomery, J. A। J.; Vreven, T.; Kudin, K. N.; Burant, J. C.; Millam, J. M.; Iyengar, S. S.; Tomasi, J.; Barone, V.; Mennucci, B.; Cossi, M.; Scalmani, G.; Rega, N.; Petersson, G. A.; Nakatsuji, H.; Hada, M.; Ehara, M.; Toyota, K.; Fukuda, R.; Hasegawa, J.; Ishida, M.; Nakajima, T.; Honda, Y.; Kitao, O.; Nakai, H.; Klene, M.; Li, X.; Knox, J. E.; Hratchian, H. P.; Cross, J. B.; Bakken, V.; Adamo, C.; Jaramillo, J.; Gomperts, R.; Stratmann, R. E.; Yazyev, O.; Austin, A. J.; Cammi, R.; Pomelli, C.; Ochterski, J. W.; Ayala, P. Y.; Morokuma, K.; Voth, G. A.; Salvador, P.; Dannenberg, J. J.; Zakrzewski, V. G.; Dapprich, S.; Daniels, A. D.; Strain, M. C.; Farkas, O.; Malick, D. K.; Rabuck, A. D.; Raghavachari, K.; Foresman, J. B.; Ortiz, J. V.; Cui, Q.; Baboul, A. G.;

Vibrational Coherence in Methanol Solution of ZnTMPyP

J. Phys. Chem. B, Vol. 114, No. 46, 2010 **15277**

Clifford, S.; Cioslowski, J.; Stefanov, B. B.; Liu, G.; Liashenko, A.; Piskorz, P.; Komaromi, I.; Martin, R. L.; Fox, D. J.; Keith, T.; Al-Laham, M. A.; Peng, C. Y.; Nanayakkara, A.; Challacombe, M.; Gill, P. M. W.; Johnson, B.; Chen, W.; Wong, M. W.; Gonzalez, C.; Pople, J. A. *Gaussian 03*, revision D.01; Gaussian, Inc.: Wallingford, CT, 2004.

(37) Lakowicz, J. R. *Principles of Fluorescence Spectroscopy*, 2nd ed.; Kluwer Academic/Plenum Publishers: New York, 1999.

(38) Wang, Q.; Schoenlein, R. W.; Peteanu, L. A.; Mathies, R. A.; Shank, C. V. Vibrationally coherent photochemistry in the femtosecond primary event of vision. *Science* **1994**, *266*, 422–424.

(39) Cantor, C. R.; Schimmel, P. R. *Biophysical Chemistry. Part II: Techniques for the Study of Biological Structure and Function*; W. H. Freeman and Company: San Francisco, 1980.

(40) McHale, J. L. *Molecular Spectroscopy*; Prentice Hall: Upper Saddle River, NJ, 1999.

(41) Cong, P.; Deuhl, H. P.; Simon, J. D. Using optical coherence to measure the ultrafast electronic dephasing of large molecules in room-temperature liquids. *Chem. Phys. Lett.* **1993**, *212*, 367–373.

(42) Joo, T.; Jia, Y.; Yu, J.-Y.; Lang, M. J.; Fleming, G. R. Third-order nonlinear time domain probes of solvation dynamics. *J. Chem. Phys.* **1996**, *104*, 6089–6108.

(43) Xu, Q.; Ma, Y.; Stiopkin, I. V.; Fleming, G. R. Wavelength-dependent resonant homodyne and heterodyne transient grating spectroscopy with a diffractive optics method: Solvent effect on the third-order signal. *J. Chem. Phys.* **2002**, *116*, 9333–9340.

(44) Press, W. H.; Flannery, B. P.; Teukolsky, S. A.; Vetterline, W. T. *Numerical Recipes: The Art of Scientific Computing*; Cambridge University Press: Cambridge, U.K., 1986.

(45) Stratt, R. M. The instantaneous normal modes of liquids. *Acc. Chem. Res.* **1995**, *28*, 201–207.

(46) Stratt, R. M.; Maroncelli, M. Nonreactive dynamics in solution: The emerging molecular view of solvation dynamics and vibrational relaxation. *J. Phys. Chem.* **1996**, *100*, 12981–12996.

(47) Enescu, M.; Steenkeste, K.; Tfibel, F.; Fontaine-Aupart, M.-P. Femtosecond relaxation processes from upper excited states of tetrakis(*N*-methyl-4-pyridyl)porphyrins studied by transient absorption spectroscopy. *Phys. Chem. Chem. Phys.* **2002**, *4*, 6092–6099.

(48) Pollard, W. T.; Lee, S.-Y.; Mathies, R. A. Wave packet theory of dynamic absorption spectra in femtosecond pump-probe experiments. *J. Chem. Phys.* **1990**, *92*, 4012–4029.

(49) Blom, N.; Odo, J.; Nakamoto, K.; Strommen, D. P. Resonance Raman studies of metal tetrakis(4-*N*-methylpyridyl)porphine: Band assignments, structure-sensitive bands, and species equilibria. *J. Phys. Chem.* **1986**, *90*, 2847–2852.

(50) Franzen, S.; Fritsch, K.; Brewer, S. H. Experimental observation of anharmonic coupling of the heme-doming and iron-ligand out-of-plane vibrational modes confirmed by density functional theory. *J. Phys. Chem. B* **2002**, *106*, 11641–11646.

(51) London, F. The general theory of molecular forces. *Trans. Faraday Soc.* **1937**, *33*, 8–26.

(52) Margenau, H. van der Waals forces. *Rev. Mod. Phys.* **1939**, *11*, 1–35.

(53) Kauzmann, W. *Quantum Chemistry: An Introduction*; Academic Press: New York, 1957.

(54) Berry, R. S.; Rice, S. A.; Ross, J. *Physical Chemistry*; Oxford University Press: New York, 2000.

(55) Lide, D. R., Ed. *CRC Handbook of Chemistry and Physics*; CRC Press, Inc.: Boca Raton, FL, 2006.